Dalton Transactions

ROYAL SOCIETY OF CHEMISTRY

PAPER

View Article Online
View Journal | View Issue

Cite this: *Dalton Trans.*, 2025, **54**, 10370

Efficient 0.4 μm–1.6 μm emission from muffin-shaped nine-coordinated ternary samarium(III) and erbium(III) complexes†‡

Rashid Ilmi, *[a] Sevgi Kansız,[b] Nawal K. Al Rasbi, [a] Sadiya Anjum,*[c] Rik Van Deun [d] and Muhammad S. Khan *[a]

Received 24th March 2025,
Accepted 22nd May 2025

DOI: 10.1039/d5dt00710k

rsc.li/dalton

Two nine coordinated lanthanide(III) complexes with the general formula [Ln(tfac)$_3$(tptz)] [Ln = Sm(III) (**Sm1**) or Er(III) (**Er1**); tfac is the anion of 1,1,1-trifluoro-2,4-pentanedione and tptz = 2,4,6-tri(2-pyridyl)-1,3,5-triazine] exhibiting emissions in the visible to near-infrared (NIR) region of the electromagnetic (EM) spectrum were synthesized. The molecular structure of the complexes was established using the single-crystal X-ray diffraction (SC-XRD) method, which explicitly confirms the formation of the nine-co-ordinated complexes with an LnO_6N_3 coordination sphere. Hirshfeld surface analysis reveals the presence of different non-covalent interactions (NCIs) and their role in stabilizing the molecular structure. The optical properties of **Sm1** and **Er1** were analysed and discussed in detail using UV-Vis-NIR absorption, steady-state emission and excited-state decay dynamics. Upon ligand-centred excitation, either in the solid state or in solution, **Sm1** and **Er1** exhibit their typical f–f emissions, covering a wide range of 400–1600 nm. Both complexes display a sizeable excited lifetime and fall in the category of efficient lanthanide materials. A possible emission mechanism involved in the sensitized visible and NIR emission is also proposed based on the available data set.

Introduction

The design and synthesis of NIR emitting lanthanide(III) complexes are of paramount interest owing to their potential applications in diverse fields, such as NIR organic light-emitting diodes (OLEDs),[1] which could be utilized in wireless data transmission, pulse oximeters, imaging,[2] sensors,[3] and other applications. The emission of lanthanide (Ln) ions originates from intra-configurational 4f–4f transitions, which are forbidden by Laporte's rule ($\Delta L = \pm 1$) and the spin rule ($\Delta S = 0$). Consequently, the emission exhibits low photon absorption efficiency, resulting in weak emission intensity and low quantum yield. This bottleneck can swiftly be overcome by coordinating Ln ions with a strong light absorbing sensitizing ligand(s) that channels the absorbed energy to Ln ions—called the antenna effect.[4] For this purpose, a wide variety of sensitizing oxygen (O)-donor, nitrogen (N)-donor or mixed NO-donor ligands have been employed.[5]

Among the large pool of sensitizing ligands, monoanionic bidentate β-diketones are unique; however, owing to the large ionic radius of Ln(III) ions, their coordination number is usually high, *e.g.*, eight or nine together with the valency, which cannot be satisfied by monoanionic β-diketone ligands alone.[6] Subsequently, tris β-diketonato Ln chelates are always accompanied by water/coordinating solvent(s), which drastically shorten the excited lifetime, especially in the case of NIR emitting Ln ions, such as Nd(III), Ho(III), Er(III), and Yb(III)-based complexes.[7] This is because of the small energy gap between the emitting level and the ground state of the metal centre that resulted in a vibrational quenching phenomenon, which is not only due to the high energy oscillators (O–H and N–H) directly bonded to Ln ions but also due to the unbound C–H oscillators with r^{-6} distance dependence.[8] This unavoidable detrimental effect could be partially overcome by replacing water/solvent molecules with one or more additional

[a]*Department of Chemistry, Sultan Qaboos University, P.O. Box 36, Al Khod 123, Oman. E-mail: rashidilmi@gmail.com, msk@squ.edu.om*
[b]*Department of Fundamental Sciences, Faculty of Engineering, Samsun University, Samsun, Turkey*
[c]*Applied Science and Humanities, Inderprastha Engineering College, Ghaziabad, Uttar Pradesh 201010, India. E-mail: sadiya2203@gmail.com*
[d]*L 3 – Luminescent Lanthanide Lab, Department of Inorganic and Physical Chemistry, Ghent University, Krijgslaan 281-S3, B-9000 Ghent, Belgium*

†The work is dedicated to my (Dr. R. Ilmi) doctoral mentor, late Professor Khalid Iftikhar (1958–2023), Jamia Millia Islamia, India, a remarkable and extraordinarily passionate inorganic chemist, for introducing me to the intriguing world of lanthanide coordination chemistry.

‡Electronic supplementary information (ESI) available. CCDC 2428252 and 2428253. For ESI and crystallographic data in CIF or other electronic format see DOI: https://doi.org/10.1039/d5dt00710k

neutral N^N/N^N^N/O^O/O^O^O ligands depending on the steric demand of the employed ligand(s). This effect could also be reduced by utilizing fluorinated ligands or *via* deuteration. We recently achieved the NIR emission of Pr(III) and Nd(III) complexes by employing the hemi-fluorinated β-diketone 1,1,1-trifluoro-2,4-pentanedione (triplet state (T_{tfac}) ≈ 22 720 cm^{-1})[9] in combination with the neutral N^N^N ligand 2,4,6-tri(2-pyridyl)-1,3,5-triazine (T_{tptz} ≈ 21 277 cm^{-1})[10] and achieved longer excited state lifetimes of 2.74 ns and 10.33 μs for Pr(III) and Nd(III) complexes, respectively.[11]

Considering our experimental observations, we turned our attention to investigating the optical properties and capability of Htfac together with tptz for sensitizing pure NIR emission of Er(III)-based and a dual (red and NIR) emitting Sm(III)-based complexes, *i.e.*, [Ln(tfac)$_3$(tptz)] (Ln = Sm(III) & Er(III)) (Fig. 1). The solid-state structure of [Sm(tfac)$_3$(tptz)] (**Sm1**) and [Er(tfac)$_3$(tptz)] (**Er1**) was determined by the SC-XRD method. Hirshfeld surface analysis was employed to understand the impact of different NCIs and their role in stabilizing the structure and crystal packing. The photophysical properties of the complexes were analysed in detail using steady-state excitation and emission spectroscopy as well as by time-resolved spectroscopy and discussed in detail.

Experimental section: materials, synthesis and analyses

Metal chlorides of samarium and erbium were purchased from Strem Chemicals, Inc. USA, while other chemicals were obtained from Sigma-Aldrich and Tokyo Chemical Industry (TCI) and used as received. Solvents were pre-dried and distilled before use according to standard procedures.[12] Elemental analysis was performed using the Euro EA – CHN Elemental Analyser in the Department of Chemistry, Sultan Qaboos University.

Synthesis of the [Sm(tfac)$_3$(tptz)] (Sm1)

Sm1 was synthesized by following the method previously reported by us.[11,13] Briefly, an equimolar ethanolic solution of [Sm(tfac)$_3$(H$_2$O)$_2$] (200 mg; 0.309 mmol) and tptz (96.75 mg; 0.309 mmol) were mixed at 50 °C and the reaction mixture was left with stirring overnight. The reaction mixture was filtered and left for evaporation. The solid obtained was washed with ice-cold ethanol (5 mL × 2) followed by hexane (5 mL × 2) and dried in the air to yield 80% of **Sm1**. Single crystals suitable for SC-XRD analysis were grown by slow evaporation of ethanolic solution. Elemental analysis for $C_{33}H_{24}F_9N_6O_6Sm$: C, 42.99; H, 2.62; N, 9.12 and found C, 42.88; H, 2.67; N, 9.08.

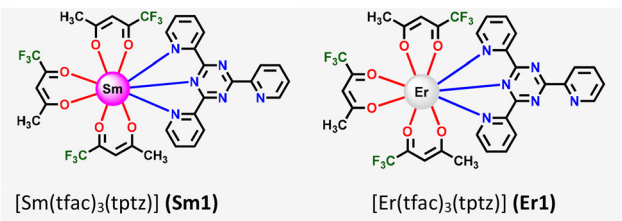

[Sm(tfac)$_3$(tptz)] **(Sm1)** [Er(tfac)$_3$(tptz)] **(Er1)**

Fig. 1 Molecular structure of the nine-coordinated complexes.

[Er(tfac)$_3$(tptz)] (Er1)

Er1 was synthesized *via* a similar method using [Er(tfac)$_3$(H$_2$O)$_2$] (200 mg; 0.301 mmol) and tptz (94.284 mg; 0.301 mmol). Single crystals suitable for SC-XRD analysis were grown by the slow evaporation of dichloromethane (CH_2Cl_2) solution. Elemental analysis for $C_{33}H_{24}F_9N_6O_6Er$: C, 42.22; H, 2.58; N, 8.95 and found C, 42.28; H, 2.65; N, 9.13.

Molecular structure determination by SC-XRD

Single crystals of **Sm1** and **Er1** with the dimensions of 0.15 × 0.15 × 0.1 mm and 0.25 × 0.2 × 0.2 mm, respectively, were selected for X-ray diffraction analysis. Intensity data were collected at 296 K using a STOE IPDS2[14] diffractometer equipped with graphite-monochromated Mo-Kα radiation (λ = 0.71073 Å). The structures were solved using direct methods with SHELXT[15] and refined by full-matrix least-squares techniques on F^2 with SHELXL-2018.[16] Molecular geometry calculations and visualizations were performed using Mercury[17] and PLATON.[18] Figures for publication were prepared through WinGX.[19] Detailed crystal data, data collection, and refinement parameters for **Sm1** and **Er1** are presented in Table S1, ESI.‡ Crystallographic data have been deposited with the Cambridge Crystallographic Data Centre (CCDC) as supplementary publication with CCDC numbers 2428252 (**Sm1**) & 2428253 (**Er1**).‡

Hirshfeld surface analysis

The Hirshfeld surfaces[20] and two-dimensional (2D) fingerprint plots were generated and analysed using the CrystalExplorer program,[21] with a crystallographic information file (CIF) serving as the input. The Hirshfeld surfaces were mapped based on the normalized contact distance (d_{norm}), calculated using the parameters d_e, d_i and r^{vdW}, as described in eqn (1).

$$d_{norm} = \frac{d_i - r_i^{vdw}}{r_i^{vdw}} + \frac{d_e - r_e^{vdw}}{r_e^{vdw}} \quad (1)$$

The d_{norm} values are visually represented on the surface using three distinct colours: red, blue, and white. Red spots indicate regions where the intermolecular contact distances are shorter than the sum of the van der Waals radii, signifying strong interactions. Blue spots correspond to regions with longer contact distances, and white regions represent contact distances approximately equal to the sum of the van der Waals radii.

Spectroscopic measurements

All spectroscopic measurements were performed at RT. The electronic absorption spectrum in the region between 200 and 1600 nm for **Sm1** and **Er1** was obtained on a Varian Cary 5000 spectrophotometer. Excitation, emission spectra and decay curves of **Sm1** and **Er1** were recorded on an Edinburgh

Instruments FLSP920 UV-vis-NIR spectrometer setup. A 450 W xenon (Xe) arc lamp was used as the steady-state excitation source. Luminescence decay times were recorded using a 60 W pulsed Xe lamp, operating at a frequency of 100 Hz or a Continuum Surelite I laser (450 mJ @1064 nm), operating at a repetition rate of 10 Hz, using the third harmonic (355 nm) as the excitation source, and the photomultiplier detectors mentioned below. A Hamamatsu R928P photomultiplier tube was used to detect the emission signals in the visible range, while a Hamamatsu R5509-72 photomultiplier was used to detect emissions in the NIR region. Powders were put between quartz plates (Starna cuvettes for powder samples, type 20/C/Q/0.2). All of the excitation spectra are recorded, observing the strongest f–f emission peak. The emission spectra reported in the study have been corrected for detector response.

Results and discussion

Synthesis, characterization and structural analysis

The complexes **Sm1** and **Er1** were synthesized by a solvothermal mixing of an equimolar amount of $[Ln(tfac)_3(H_2O)_2]$ (Ln = Sm/Er) and tptz. The proposed empirical formula was confirmed by elemental analyses, which agrees well with the proposed molecular structure shown in Fig. 1. The molecular formula was confirmed by the SC-XRD studies, which revealed that both **Sm1** and **Er1** are mononuclear and crystallize in the triclinic $P\bar{1}$ space group with a unit cell containing two formula units (Z = 2). The structures feature similar coordination environments and supramolecular interactions, yet they exhibit subtle differences due to the different metal (Sm/Er) ions. The molecular structures of **Sm1** and **Er1** are displayed in Fig. 2, while the selected bond lengths and bond angles are summarized in Table 1. As can be seen from Fig. 2, the central metal (Sm/Er) ions are nine-coordinated with the coordination sphere composed of three pairs of O-atoms from the three monoanionic bidentate tfac ligands and three N-atoms from the tridentate tptz ligand. For **Sm1**, the Sm–O bond lengths lie in the range of 2.294 to 2.425(10) Å, while Sm–N bond lengths are slightly less, from 2.558(8) to 2.583(10) Å (Table 1). For **Er1**, the Er–O bond length follows the same trend, *i.e.*, 2.305 to 2.453(7) Å and Er–N bond lengths ranging from 2.558(8) to 2.606(9) Å (Table 1). The distance between the two metal centers, *i.e.*, Sm···Sm and Er···Er in a unit cell are nearly identical [8.35 Å (**Sm1**) *vs.* 8.34 Å, (**Er1**)], which is sufficiently large to inhibit non-radiative energy migration between them and suggest similar constraints on energy migration between the metal centres in both complexes. This is beneficial for applications requiring localized luminescence properties, such as in photonic devices or sensors. Additionally, both complexes exhibit weak π···π stacking interactions between adjacent pyridine rings, which contributes to the stability of the crystal structure (Fig. 2c & d). The centroids of the interacting pyridine rings are separated by 3.6442(8) Å and 3.6193(9) Å, respectively, for **Sm1** and **Er1**, indicating effective proximity for such interactions. A marginal difference in centroid separation could be attributed to the subtle differences in the ionic radii and coordination preferences of Sm (III) *vs.* Er(III). Finally, the coordination geometry of **Sm1** and **Er1** has been analysed using the SHAPE 2.1 software,[22] which showed

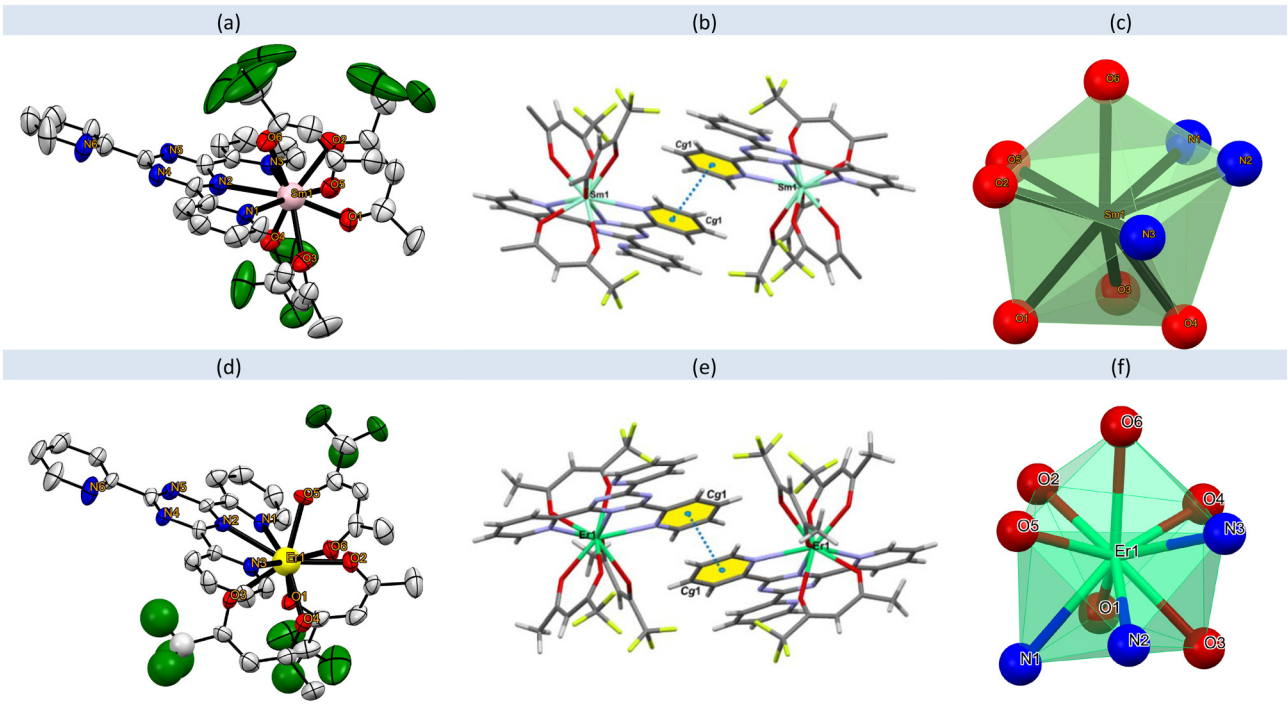

Fig. 2 Single crystal X-ray structure of (a) **Sm1**, (d) **Er1**; hydrogen and solvent molecules are omitted for clarity. Crystal packing diagram illustrating π···π interactions: (b) **Sm1** and (e) **Er1**. A view of the coordination polyhedra showing the muffin (C_s) arrangement: (c) **Sm1** and (f) **Er1**.

Table 1 Some selected geometric parameters for **Sm1** and **Er1**

Bond length	Value (Å)	Bond angle	Value (°)	Bond length	Value (Å)	Bond angle	Value (°)
	Sm1				**Er1**		
Sm1–O1	2.299(9)	O1–Sm1–O2	71.1(4)	Er1–O1	2.396(7)	O1–Er1–O2	70.6(3)
Sm1–O2	2.392(10)	O1–Sm1–O4	77.1(3)	Er1–O2	2.316(8)	O1–Er1–O4	74.2(3)
Sm1–O3	2.425(10)	O1–Sm1–O6	138.7(3)	Er1–O3	2.337(8)	O1–Er1–O6	132.4(3)
Sm1–O4	2.294(10)	O2–Sm1–O4	122.4(3)	Er1–O4	2.309(8)	O2–Er1–O3	138.4(4)
Sm1–O5	2.325(9)	O4–Sm1–O5	144.8(3)	Er1–O5	2.305(7)	O2–Er1–O4	81.4(3)
Sm1–O6	2.343(9)	N1–Sm1–N2	62.3(3)	Er1–O6	2.453(7)	N1–Er1–N2	62.9(3)
Sm1–N1	2.583(10)	N1–Sm1–N3	125.5(3)	Er1–N1	2.597(9)	N1–Er1–N3	125.4(3)
Sm1–N2	2.558(10)	N2–Sm1–N3	62.9(3)	Er1–N2	2.558(8)	N1–Er1–O2	93.9(3)
Sm1–N3	2.567(10)	N1–Sm1–O2	135.6(4)	Er1–N3	2.606(9)	N1–Er1–O4	143.5(3)

that both complexes acquired a muffin shape (Fig. 2e & f) with approximate C_s symmetry and deviations of 0.761 and 0.901, respectively, from the idealized muffin geometry (Table S2, ESI‡).

The Hirshfeld surface visualizations of d_{norm}, shape index and curvedness are employed to underpin the role of different NCIs and molecular arrangements within the crystal lattice.[23] Fig. 3a illustrates the Hirshfeld surface maps of **Sm1** and **Er1**, showcasing the d_{norm}, shape index, and curvedness distributions. The d_{norm} function provides a fundamental visualization of contact areas, highlighting regions where the NCI distances are shorter than the sum of the van der Waals radii, which are depicted in red. For the **Er1**, the d_{norm} values range

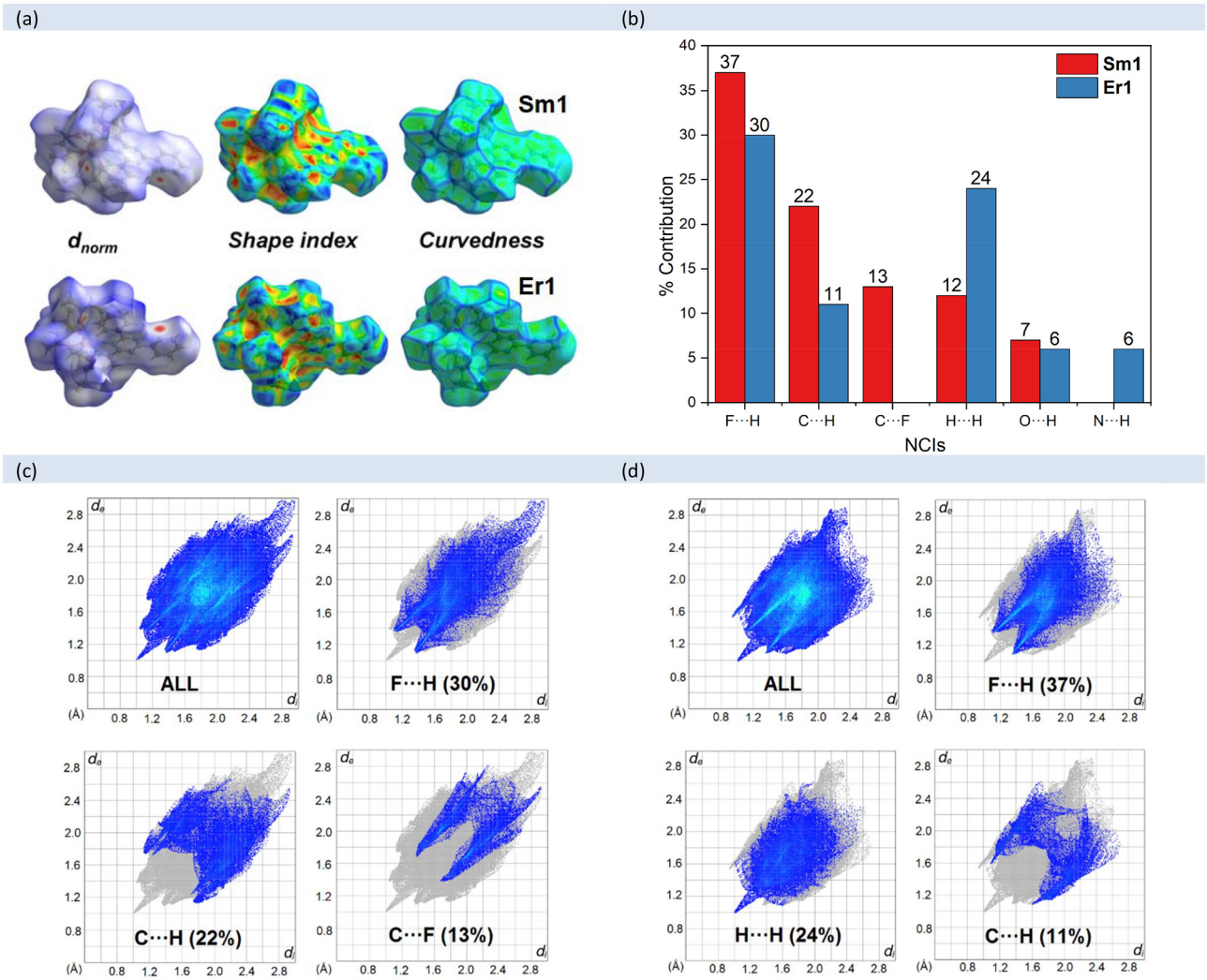

Fig. 3 (a) Hirshfeld surfaces with d_{norm}, shape index and curvedness maps. (b) 2D fingerprint plots and percentage contributions of different NCIs for (c) **Sm1** and (d) **Er1**.

between 0.2489 and 1.4353 Å, while for **Sm1**, they range between −0.1292 and 2.1221 Å. The shape index ranges from −1 to 1, while curvedness values vary between −4 and 4. The shape index provides information about the planar π···π interactions between molecules, depicted as alternating red and blue triangular features on the surface. Curvedness, on the other hand, measures the global curvature of the surface, enabling the identification of regions associated with hydrogen bonds or other types of significant NCIs. The 2D fingerprint plots provide a detailed analysis of the contribution of various NCIs within the crystal structure. These plots graphically represent the relationship between d_e and d_i, offering a comprehensive overview of the NCI patterns present in the crystal. Fig. 3b and c provide a detailed breakdown of the contributions of various NCIs to the Hirshfeld surface area of **Sm1** and **Er1**. An analysis of the data reveals that the F···H contacts contribute the most to the total surface area and account for 30% and 37% for **Sm1** and **Er1**, respectively. For **Er1**, H···H contacts constitute 24% of the surface area, while C···H contacts contribute 11%. Other significant contributions include O···H contacts at 6.0% and N···H contacts at 6.0%. Minor contributions were observed from C···C contacts (2.8%), C···F contacts (2.8%), C···N contacts (2.5%), and F···F contacts (1.6%) (Fig. 3c). Similarly, for **Sm1**, C···H contacts contribute 22% of the surface area, while C···F contacts account for 13%. Notable contributions also include H···H contacts at 12% and O···H contacts at 7%. Minor contributions come from C···C contacts (6%). These findings emphasize that the crystal packing of both complexes is predominantly stabilized by F···H contacts, underscoring the critical role of hydrogen bonding interactions in their structural organization.

Photophysical properties of the complexes

UV-Visible-NIR optical absorption spectroscopy. The optical absorption spectra of **Sm1** and **Er1** together with their binary hydrated complexes ([Sm(tfac)$_3$(H$_2$O)$_2$] and [Er(tfac)$_3$(H$_2$O)$_2$]) and free tptz in dilute CH_2Cl_2 are shown in Fig. 4a. The absorption spectrum of **Sm1** and **Er1** in the UV region exhibi-

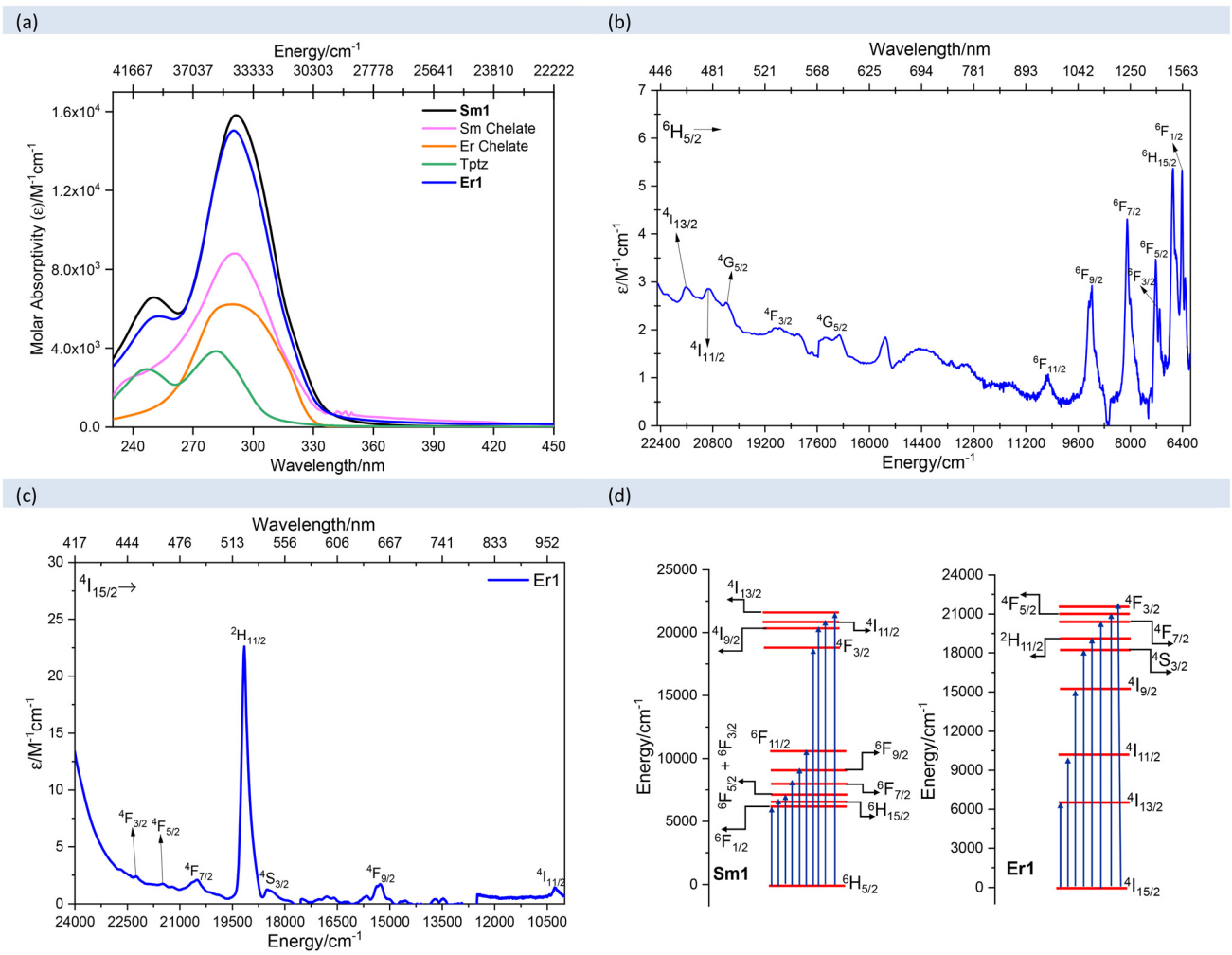

Fig. 4 UV-visible absorption spectra of (a) **Sm1** and **Er1** together with those of the free tptz and binary hydrated complexes (c = 1 × 10^{-5} M) in CH_2Cl_2. Visible to NIR absorption spectrum of (b) **Sm1** (c = 3.2 × 10^{-3} M) and (c) **Er1** (c = 3.15 × 10^{-3} M) and (d) different transitions originating from the ground $^6H_{5/2}$ and $^4I_{15/2}$ states to various excited states of Sm(III) and Er(III), respectively, in CH_2Cl_2.

ted combined absorption bands of both primary Htfac and ancillary tptz ligands ([Sm(tfac)$_3$(H$_2$O)$_2$]; 290; ε = 8860 M^{-1} cm^{-1}, [Er(tfac)$_3$(H$_2$O)$_2$]; 289 nm; ε = 6202 M^{-1} cm^{-1} and tptz; 246 nm; ε = 2962 M^{-1} cm^{-1} and 281 nm; ε = 3880 M^{-1} cm^{-1}) with the λ_{abs}^{max} = 292 nm ($\varepsilon \approx$ 15 832 M^{-1} cm^{-1}) and 290 nm ($\varepsilon \approx$ 15 045 M^{-1} cm^{-1}) for **Sm1** and **Er1**, respectively. The absorption spectrum in the region between 225 and 400 nm is almost identical, implying that they have nearly identical geometries, which is indeed the case as determined by SC-XRD studies. Both complexes also exhibited faint 4f–4f electronic transitions originating from the $^6H_{5/2}$ and $^4I_{15/2}$ ground states to various excited states of Sm(III) and Er(III), respectively. To identify and detect potential absorption transitions and present a clear view, the concentration of the solution was increased as the 4f–4f absorption transitions have very low oscillator strengths (O.S. $\approx 10^{-6}$).[25] The intensity of the absorption transitions can be expressed in terms of O.S. (P × 10^{-6}), which is experimentally related to the integrated area of the absorption band and is expressed by the following eqn (2).[26]

$$P = 4.31 \times 10^{-9} \times \left[\frac{9\eta}{(9\eta+2)^2}\right] \int \varepsilon(\upsilon)\mathrm{d}\upsilon \qquad (2)$$

where η is the refractive index of the solution and $\varepsilon(\upsilon)$ is the molar extinction coefficient at wavelength υ. The O.S. of the transitions is determined by evaluating the area under the peak.

The absorption transitions observed in the present **Sm1** and **Er1** are assigned based on the work by Carnall.[24] The data obtained for **Sm1** and **Er1**, such as transitions with their respective energies and O.S., is given in Table 2, and the absorption spectra are shown in Fig. 4(b–d). As can be seen from Table 2, **Sm1** displayed the two strongest transitions, $^6F_{9/2}$ (5.20 × 10^{-6}) and $^6F_{7/2}$ (5.43 × 10^{-6}), in the NIR region while **Er1** exhibited the strongest transition due to $^2H_{11/2}$ in the visible region at 19 147 cm^{-1} with O.S. $\approx$ 70.11 × 10^{-6} due to its hypersensitive nature[27] and is ≈24-folds higher than Er(III)-aqua ion (2.91 × 10^{-6}).[25]

Visible and NIR emission of Sm1. For lanthanide complexes with efficient emissions, the coordinated organic ligands should fulfil necessary conditions, including strong light absorption properties, *i.e.*, high ε and appropriate energy differences (ΔE)[28] between the T of coordinated organic ligand (s) and the emitting levels of Ln(III) ions. As can be seen from Fig. 4a, both the complexes exhibit good ε in the region between 225 and 350 nm. The ΔE was calculated from the difference between the T states of the coordinated organic ligand(s), which lies at $T_{tfac} \approx$ 22 720 cm^{-1} [9] and $T_{tptz} \approx$ 21 277 cm^{-1} (ref. 10) and emitting levels of Sm(III). The excited states $^4G_{5/2}$ (≈17 355 cm^{-1}), $^4F_{3/2}$ (≈18 805 cm^{-1}) and $^4G_{7/2}$ (≈20 cm^{-1})[24] of Sm(III) are potential candidates (Fig. 5d) to receive the energy from the T states of the coordinated organic ligand(s);[29] however, the emission for Sm(III)-based complexes originates from $^4G_{5/2}$ (≈17 924 cm^{-1}). It is a general mandate that after receiving the energy, $^4G_{7/2}$ transfers it to $^4F_{3/2}$, which finally relaxes the absorbed energy to the $^4G_{5/2}$ state, which in turn, undergoes radiative processes leading to emission from the $^4G_{5/2}$ state[30] as shown in Fig. 5c. The calculated values of $\Delta E(T - {}^4G_{5/2})$ are 4796 and 3353 cm^{-1}, respectively, for Htfac and tptz, suggesting that the present **Sm1** should show good emission at room temperature.

Room-temperature excitation and emission spectra of **Sm1** in CH_2Cl_2 solution are shown in Fig. 5. The excitation spectra were obtained by monitoring the visible ($^4G_{5/2} \rightarrow {}^6H_{9/2}$) and NIR ($^4G_{5/2} \rightarrow {}^6F_{5/2}$) transitions and are identical, exhibiting intense broad ligands in the range of 250–450 nm with very faint intra-configurational 4f–4f transitions (Fig. 5a). Moreover, the higher intensity of ligand absorption over the intra-configurational 4f–4f transitions coupled with the absence of any residual ligand emission in the PL spectra points towards an efficient antenna effect. The trivalent Sm ion-based materials are very interesting since their emission spans from the visible to NIR region, covering the 400–1400 nm range of the EM spectrum. Despite this appealing feature, reports on dual emission of Sm-based materials are scarce.[8,31] The emission spectra in the visible and NIR regions of the spectrum are obtained by

Table 2 Room temperature 4f–4f electronic transitions with their energies and O.S. in the UV-Vis-NIR region in CH_2Cl_2

Sm1 (ground state $^6H_{5/2}\rightarrow$)			**Er1** (ground state $^4I_{15/2}\rightarrow$)		
Transitions	Energy (cm^{-1})	O.S. ($P \times 10^{-6}$)	Transitions	Energy (cm^{-1})	O.S. ($P \times 10^{-6}$)
$^4I_{13/2}$	21 623 [21 650]	[a]	$^4F_{3/2}$	22 296 [22 645]	[a]
$^4I_{11/2}$	20 932 [21 096]	[a]	$^4F_{5/2}$	21 482 [22 100]	[a]
$^4G_{7/2}$	20 381 [20 014]	[a]	$^4F_{7/2}$	20 503 [20 450]	4.79
$^4F_{3/2}$	18 805 [18 832]	[a]	$^2H_{11/2}$	19 147 [19 150]	70.11
$^4G_{5/2}$	17 355 [17 924]	[a]	$^4S_{3/2}$	18 486 [18 350]	9.450
$^6F_{11/2}$	10 561 [10 517]	[a]	$^4F_{9/2}$	15 298 [15 250]	4.23
$^6F_{9/2}$	9175 [9136]	5.20	$^4I_{11/2}$	10 263 [10 250]	0.800
$^6F_{7/2}$	8067 [7977]	5.43			
$^6F_{5/2} + {}^6F_{3/2}$	7208 & 7067	2.84			
$^6H_{15/2}$	6701 [6508]	3.14			
$^6F_{1/2}$	6376 [6397]	1.80			

Values in the square parentheses are for Sm(II) and Er(III) aqua-ion taken from Ref. 24. [a] O.S. not determined due to the very weak and slanting nature of the transitions.

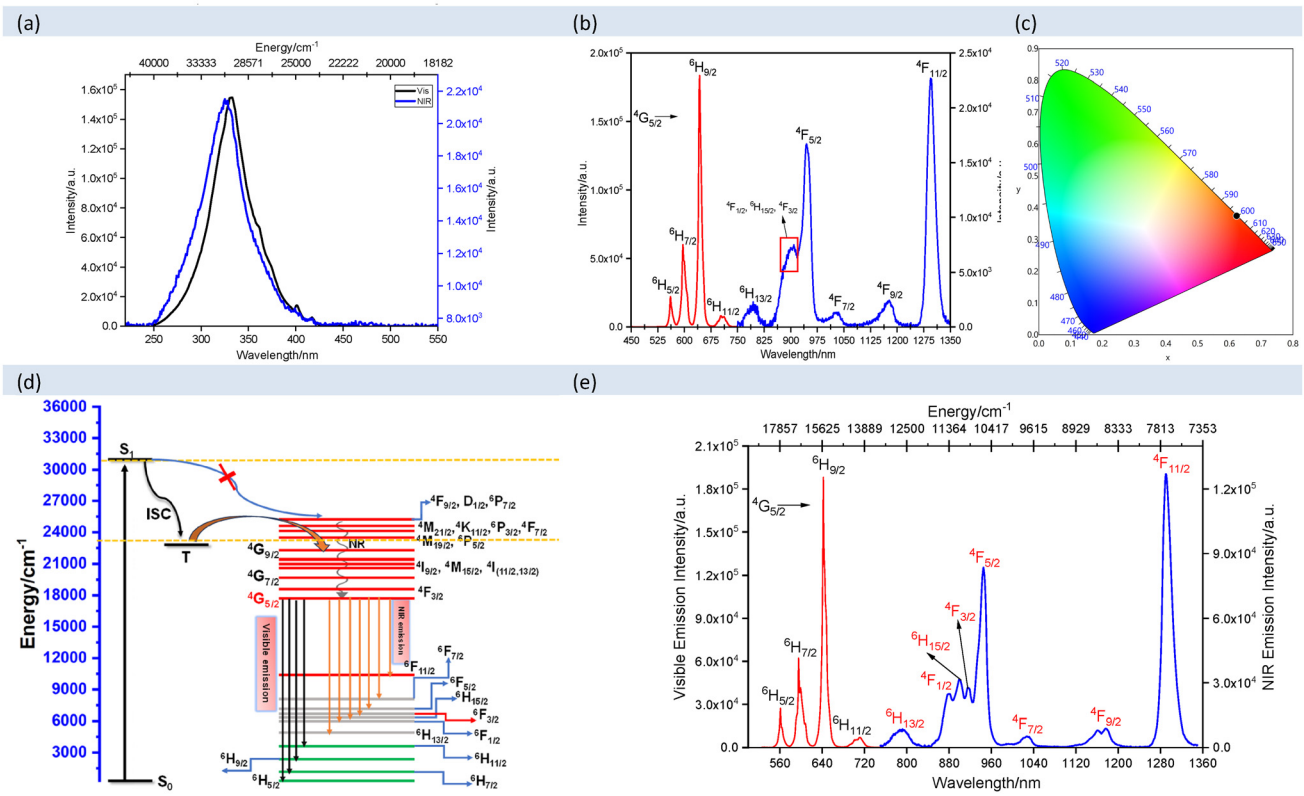

Fig. 5 Room temperature (a) excitation and (b) emission spectra of **Sm1** in the visible and NIR regions in CH_2Cl_2, (c) CIE colour coordinate diagram of visible emission, (d) energy migration pathway for **Sm1** and (e) solid-state emission spectrum of **Sm1**.

exciting **Sm1** at λ_{ex}^{max} and is shown in Fig. 5b. The complex exhibits typical emission transitions originating from the $^4G_{5/2}$ levels. In the visible region of the spectrum, the complex exhibits four transitions from the $^4G_{5/2}$ level to the different J levels of the ^6H_J term (J = 5/2, 7/2, 9/2, & 11/2).

The transition appearing at 17 857 cm^{-1} (561 nm) has a magnetic-diploe (MD) $^4G_{5/2} \rightarrow {}^6H_{5/2}$ characteristic ($\Delta J = 0$) and is taken as a reference to determine the percentage (%) contribution of each transition to the overall emission. The data obtained are summarized in Table 3. As can be seen from Table 3, the electric-diploe (ED) $^4G_{5/2} \rightarrow {}^6H_{9/2}$ transition appearing at 15 552 cm^{-1} (643 nm) dominates the spectrum covering 60.38% of the total integrated emission intensity and is responsible for monochromatic red emission (FWHM = 9.47 nm) as reflected by the CIE colour coordinates ($CIE_{x,y}$ = 0.62; 0.37, Fig. 5c) with a colour purity of 88.00%. The intensity of the transitions follows the order: $^4G_{5/2} \rightarrow {}^6H_{9/2} > {}^4G_{5/2} \rightarrow {}^6H_{7/2} \gg {}^4G_{5/2} \rightarrow {}^6H_{5/2} \gg {}^4G_{5/2} \rightarrow {}^6H_{11/2}$. The intensity parameter (η_{Sm}),[32] which is the ratio between the intensities of the $^4G_{5/2} \rightarrow {}^6H_{9/2}$ and $^4G_{5/2} \rightarrow {}^6H_{5/2}$, was calculated and provides information about the polarizability of the chemical environment of the Sm(III) ion. The high experimental η_{Sm} = 7.91 for **Sm1** suggests a low symmetry of the coordination sphere and corroborates well the SC-XRD result. Under the same excitation, **Sm1** also exhibited NIR emission from the same $^4G_{5/2}$ excited state to different J levels of the ^6H_J term (J = 13/2 & 15/2) and the ^4F_J term (J = 5/2, 7/2, 9/2 & 11/2), which are assigned according to ref. 31*d* and is shown in Fig. 5b. The spectrum in the NIR region exhibits two strong emission peaks appearing between the first and second telecommunication windows, *i.e.*, at 10 582 cm^{-1} (945 nm; first telecommunication window) and 7710 cm^{-1} (1297 nm; second telecommunication window), corresponding to $^4G_{5/2} \rightarrow {}^4F_{7/2}$ and $^4G_{5/2} \rightarrow {}^4F_{11/2}$ transitions, respectively. The transition appearing at 9709 cm^{-1} (1030 nm) and 8525 cm^{-1} (1173 nm) assigned to $^4G_{5/2} \rightarrow {}^4F_{7/2}$ and $^4G_{5/2} \rightarrow {}^4F_{9/2}$, respectively, are in resonance with the third vibrational harmonic of CH oscillators and is least intense compared to the rest of NIR transitions. Thus, it is safe to say that the Htfac in tandem with tptz could be a potential photosensitiser to exploit the dual emitting nature of the Sm(III) ion. Moreover, we further obtained and examined the solid-state excitation (Fig. S1, ESI‡) and emission spectra of **Sm1** shown in Fig. 5e, and the data are summarized in Table 3. As observed for the solution, the solid-state excitation spectra exhibited similar characteristics except for lower intensity intraconfigurational 4f–4f transitions when monitored at the NIR ($^4G_{5/2} \rightarrow {}^6F_{5/2} \approx$ 10 627 cm^{-1}) transition (Fig. S1, ESI‡). The emission spectrum in the visible region showed identical emission bands with similar intensity trends, as noted in the case of the CH_2Cl_2 solution. The spectrum is dominated by the

Table 3 Room temperature photophysical properties of **Sm1** in the visible region in a CH_2Cl_2 solution and solid state

Transitions ($^4G_{5/2}\rightarrow$)	Barycentre/cm^{-1}	% contribution to the total Intensity[a]	η_{Sm}	τ_{obs}/μs	Q^{L}_{Sm}/%	Q^{Sm}_{Sm}/%	A_{rad}/s^{-1}	A_{nrad}/s^{-1}
		Solution/solid-state					Solution	
$^6H_{5/2}$	17 825.31/17 825.31	7.63/8.27	7.91/7.30	58.70/53.47	1.60	1.90[b]	(2.72×10^2)[c]	(1.68×10^4)[d]
$^6H_{7/2}$	16 778.52/16 806.72	60.38/60.40						
$^6H_{9/2}$	15 552.09/15 576.32	27.90/27.95						
$^6H_{11/2}$	14 224.75/14 064.70	4.07/3.38						

[a] Relative to the MD $^4G_{5/2} \rightarrow {}^6H_{5/2}$. [b] $Q^{Sm}_{Sm} = \tau_{obs}/\tau_{rad}$ [natural radiative lifetime ($(\tau_{rad}) = 3100$ μs)[33]]. [c] $A_{rad} = Q^{L}_{Sm}/\tau_{obs}$. [d] $A_{nrad} = 1/\tau_{obs} - A_{rad}$.

narrow bandwidth (FWHM = 9.10 nm) ED $^4G_{5/2} \rightarrow {}^6H_{9/2}$ transition (60.40% of the total integrated emission intensity) responsible for monochromatic red emission ($CIE_{x,y}$ = 0.62; 0.38 (Fig. S2, ESI‡) and CP = 90.00%) with similar η_{Sm} = 7.31 (Table 3). A comparative emission spectrum is also shown in Fig. S3 & S4, ESI.‡ A similar η_{Sm} value, together with the identical emission spectrum, implies that the **Sm1** did not lose its identity in solution and has similar site symmetry. The emission spectrum in the NIR region displayed the same but well-resolved emission transitions with improved intensity than the solution. The higher intensity of the solid-state emission could be due to the suppression of vibrational strength of the C–H oscillators, which is minimized by the NCIs interactions (C···H; 22% and F···H; 30%). This is further supported by the three-fold intense $^4G_{5/2} \rightarrow {}^4F_{7/2}$ and $^4G_{5/2} \rightarrow {}^4F_{9/2}$ transitions, which match the third vibrational overtone of the C–H oscillators.

Along with the steady-state emission, the emission decay dynamics of **Sm1** were also carried out in solution as well as in the solid-state (Fig. S5–S7, ESI‡) to get the information of the excited state lifetime (τ_{obs}). The decay curves in solution and in the solid state were obtained by monitoring the $^4G_{5/2} \rightarrow {}^6H_{9/2}$ (15 552 cm^{-1}) and $^4G_{5/2} \rightarrow {}^4F_{5/2}$ (10 627 cm^{-1}) transitions, and the data obtained are summarized in Table 3. In each case, the decay curves fit the mono-exponential behaviour very well, implying the presence of one-site symmetry. The complex exhibits almost similar τ_{obs} values, which are in line with the steady-state emission results. The determined τ_{obs}, in either case, displayed long values of 58.70 μs (visible) and 59.50 μs (NIR) for the solution and 53.47 μs (NIR) in the solid-state and fall in the category of efficient samarium complexes reported (Table 4). Moreover, the identical τ_{obs} values either obtained by the visible or the NIR emission transitions point to the fact that the transitions originate from the same excited state level, *i.e.*, $^4G_{5/2}$. The τ_{obs} of the present **Sm1** is eight-fold longer than that of the $[Sm(tfac)_3(H_2O)]$[34] and thus the replacement of water molecule lifts the detrimental quenching effect and generates a longer τ_{obs}. The complex in solution displayed a sizeable quantum yield (Q^{L}_{Sm}) of 1.60% and falls in the category of efficient ternary Sm(III) complexes (Table 4). From the τ_{obs} and Q^{L}_{Sm}, radiative (A_{rad}) and non-radiative (A_{nrad}) decay rates were also calculated by utilizing the following equations $A_{rad} = Q^{L}_{Sm}/\tau_{obs}$ and $A_{nrad} = 1/\tau_{obs} - A_{rad}$ and are summarized in Table 3.

Table 4 The comparative photophysical properties of **Sm1** with the reported efficient ternary Sm(III) complexes.[33,35]

Complexes	τ_{obs}/μs	Q^{L}_{Sm}/Q^{Sm}_{Sm}	Ref.
Sm1	58.70	1.60/1.90	This work
[Sm(Btfa)(DBM)(NTA)(tta)]K	127	7.2/—	35a
$[Sm(hfaa)_3$(DPEPO)]	280	5.0/—	35b
$[Sm(hfaa)_3$(tpy-HImzphen)]	41.3	4.4/—	35c
$[Sm(hfaa)_4]^-[DpaH]^+$	184.07	4.2/5.9	35d
$[Sm(hfaa)_3$(xantpo)2]	350	3.8/—	35b
$[Sm(hfaa)_3$(Py-Im)]	105.50	—/3.40	35e
$[Sm(tfaa)_3$(DPEPO)]	102.68	2.5/	35f
$[Sm(hfaa)_3$(*t*Bu-xantpo)]	150	2.4/—	35b
$[Sm(PM)_3$(TP)2]	84.7	1.8/2.7	33
$[Sm(acac)_3(Br_2$-phen)]	38.76	1.1/—	35g
$[Sm(hfaa)_3$(phen)$_2$]	56	—/1.3	35h
$[Sm(fod)_3(im)_2]$	33.59	—/1.03	35i

Anion of HBtfa = 4,4,4-trifluoro-1-phenyl-1,3-butanedione; HDBM = 1,3-diphenylpropane-1,3-dione; HNTA = 4,4,4-trifluoro-1-(naphthalen-2-yl)butane-1,3-dione; Htta = 4,4,4-trifluoro-1-(thiophen-2-yl)butane-1,3-dione; Hhfaa = hexafluoroacetylacetone; Hacac = acetylacetone; PM = 1-phenyl-3-methyl-4-isobutyryl-5-pyrazolone; Hfod = 6,6,7,7,8,8,8-heptafluoro-2,2-dimethyl-3,5-octanedione. Neutral ligands: DPEPO = Bis[2-(diphenylphosphino)phenyl] ether oxide; tpy-HImzphen = 2-(4-[2,2′:6′,2″] terpyridin-4′-yl-phenyl)-1*H*-phenanthro[9,10-*d*]imidazole; xantpo = 4,5-bis (diphenylphosphoryl)-9,9-dimethylxanthene; Dpa = 2,2′-dipyridylamine; Py-IM = 2-(2-pyridyl)benzimidazole; *t*Bu-xantpo = 4,5-bis(di-*tert*-butylphosphoryl)-9,9-dimethylxanthene; TP = triphenyl phosphine oxide; Br_2-phen: 4,7-dibromo-1,10-phenanthroline; Phen = 1,10-phenanthroline; im = imidazole.

The A_{nrad} is almost 61-fold higher than A_{rad} and is due to the small energy gap between the emitting level and the next lower energy level (7400 cm^{-1}), along with the presence of a high-energy oscillator. The intrinsic quantum yield (Q^{Sm}_{Sm}) was also calculated by utilizing the literature value of natural radiative lifetime (3100 μs).[33] The Q^{Sm}_{Sm} of the **Sm1** is 1.2-fold higher than Q^{L}_{Sm}.

NIR emission of Er1. Room-temperature excitation and emission spectra of **Er1** in the solid state and CH_2Cl_2 solution are shown in Fig. 6a and Fig. S8, ESI.‡ The excitation spectra were obtained by monitoring the $^4I_{13/2} \rightarrow {}^4I_{15/2}$ transition at 1524 nm (6561 cm^{-1}) and show similar broadband (except for the change in intensity) in the region of 250 and 425 nm, corresponding to the $\pi \rightarrow \pi^*$ electronic transitions of the ligands, together with the intra-configurational 4f–4f transitions. The transitions originate from the $^4I_{15/2}$ ground level

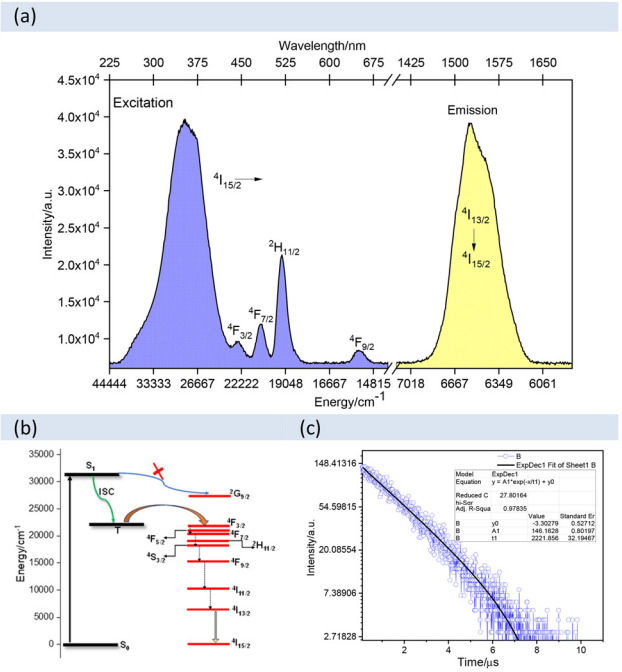

Fig. 6 (a) Solid-state excitation and emission spectra of **Er1**, (b) a partial energy level diagram showing the possible energy migration pathway and (c) transient decay profile together with the fitted curve and fitting details.

Table 5 Photophysical properties of **Er1** and Er(III) analogues[38]

Complexes	FWHM/ nm	τ_{obs}/ μs	Q_{Er}^{Er} (%)	Ref.
Er1	80/81	2.22/1.65	0.11/0.08	This work
[Er(btfa)$_3$bpy]	76	1.19	0.0085	38a
[Er(btfa)$_3$Phen]	78	2.06	0.0147	38a
[Er(btfa)$_3$(dpq)]	82	3.26	0.023	38a
[Er(btfa)$_3$(dppz)]	79	4.53	0.032	38a
[Er(tpm)$_3$(5-NO$_2$phen)]	—	1.53	0.0765[a]	38b
[Er(tpm)$_3$(bipy)]	—	1.77	0.0885[a]	38b
[Er(tpm)$_3$(bath)]	—	1.55	0.0775[a]	38b
[Er(tfac)$_3$(bpy)]	—	1.65	0.0825[a]	38c
[Er(tfac)$_3$(bath)]	—	1.40	0.07[a]	38c
[Er(tfac)$_3$(5-NO$_2$phen)]	—	1.35	0.0675[a]	38c
[Er(dmh)$_3$(bpy)]	65	1.67	0.0835[a]	38d
[Er(dmh)$_3$(bath)]	60	1.69	0.0845[a]	38d
[Er(dmh)$_3$(5-NO$_2$phen)]	58	1.38	0.069[a]	38d
[Er(dnm)$_3$(5NO$_2$phen)]	—	1.57	0.0785[a]	38e
[Er(tpm)$_3$(bath)]	—	1.53	—	38f
[Er(btfa)$_3$(me-phen)]	—	1.16	0.008	38g
[Er(tta)$_3$(pyz)]	—	1.30	0.009	38g
[Er(fod)$_3$(bath)]	—	1.39	—	38h
[Er(fod)$_3$(bpy)]	—	1.50	—	38h

[a] The authors had generalized the Q_{Er}^{Er} to 0.1%. The values shown are re-calculated using the authors' method. Anions of Htpm = 1,1,1-trifluoro-5,5-dimethyl-2,4-hexanedione; Hdmh = 2,6-dimethyl-3,5-heptanedione; Hdnm = dinaphthoylmethane. Neutral ligands: bpy = 2,2′-bipyridine, dpq/pyz = pyrazino[2,3-*f*][1,10]phenanthroline; dppz = dipyrido[3,2-*a*:2′,3′-*c*]phenazine; 5-NO$_2$phen = 5-nitro-1,10-phenanthroline, bath = bathophenanthroline; me-phen = 5-methyl-1,10-phenanthroline.

of Er(III) and are assigned to $^4F_{3/2}$ (443 nm), $^4F_{7/2}$ (481 nm), $^2H_{11/2}$ (517 nm) and $^4F_{9/2}$ (648 nm). Moreover, the intensity of the transitions is lower than that of the ligand-based broad-band, implying the role of the antenna effect in sensitizing the Er(III) emission. Under the ligand excitation (solid-state and CH_2Cl_2), **Er1** exhibited a typical NIR $^4I_{13/2} \rightarrow {}^4I_{15/2}$ transition, which covers a large spectral range of 1400–1650 nm with maxima at 1524 nm (6561 cm^{-1}) and FWHM of 80 nm for solid and 81 nm for DCM solution, respectively. The large FWHM is in line with the reported analogues and suggests that it can be utilized in a wide gain bandwidth for optical amplification applications. As mentioned above, the efficiency of energy transfer depends on the ΔE between the T states of the coordinated organic ligand(s): $T_{tfac} \approx 22\,720$ cm^{-1} [9] and $T_{tptz} \approx 21\,277$ cm^{-1},[10] which are in good resonance with the $^4F_{7/2}$ (20 790 cm^{-1}), $^2H_{11/2}$ (19 342 cm^{-1}) and $^4S_{3/2}$ (18 486 cm^{-1}). After receiving the resonate energy, it is believed that $^4F_{7/2}$ (20 790 cm^{-1}) relaxes the energy in a cascading manner to $^2H_{11/2}$, $^4S_{3/2}$, $^4F_{9/2}$, $^4I_{11/2}$ and $^4I_{13/2}$,[36] which finally emits the sensitized NIR emission (Fig. 6b). Moreover, the intensity of the solid-state emission is almost 4-fold higher than that in solution. It is important to highlight that the gap between the $^4I_{13/2}$ and $^4I_{15/2}$ states (≈6000 cm^{-1}) is in resonance to the second overtone of C–H (≈3000 cm^{-1}), N–H (≈3400 cm^{-1}) and O–H (≈3600 cm^{-1}) oscillators even in the presence of C=O (≈1700 cm^{-1}), C=N (≈1690 cm^{-1}) and C=C (≈1600 cm^{-1}) in proximity to the metal centre, which are efficient quenchers in the case of Er(III) since they require less than five overtones.[37] Thus, the higher emission intensity in the solid state could be attributed to the presence of NCIs (H···H contacts ≈24%; C···H contacts ≈11%), which suppresses the role of the high-energy oscillator.

The emission decay dynamics of **Er1** were also investigated in the solid state and in solution (Fig. 6c and Fig. S9, ESI‡) and obtained by monitoring the 1.5 μm transition. The decay curves fit mono-exponential, which gives rise to a τ_{obs} of 2.22 μs and 1.65 μs for the solid-state and CH_2Cl_2 solution, respectively, and are in line with the values for the reported ternary Er-complexes (Table 5).[38] The good fit to a mono-exponential function supports the presence of the one-site symmetry. Taking this into account the τ_{rad} of Er(III) ranging 2000–3000 μs [38d], the Q_{Er}^{Er} is 0.11% and 0.08%.

Conclusions

In summary, we successfully synthesized nine-coordinated visible and NIR-emitting **Sm1** and NIR telecom-C band-emitting **Er1**. Their molecular structures were determined by the SC-XRD method, which revealed that both complexes are nine-coordinated, and the LnO_6N_3 coordination polyhedra acquired a muffin shape with a low C_s symmetry point group. Moreover, HSA emphasized that the crystal packing of **Sm1** and **Er1** is mainly stabilized by F···H contacts and underscores the important role of hydrogen bonding interactions in structural organization. A systematic investigation and analysis of the optical

properties of **Sm1** and **Er1** coupled with our previous report on dual emission (visible and NIR) of Pr(III) and NIR emission of Nd(III) analogues unambiguously demonstrate that Htfac in tandem with the tptz ligand is an effective sensitizer for dual emission of Sm(III) and NIR emission of Er(III). Interestingly, the **Sm1** broad NIR emission covers the first (0.8–0.9 μm) and second (O band; 1.3 μm) telecom windows, while the **Er1** emission at around 1.5 μm covers the third telecom window and may provide potential material for optical fibre communications.

Data availability

The data supporting this article have been included as part of the ESI.‡

Conflicts of interest

There are no conflicts to declare.

Acknowledgements

MSK acknowledges His Majesty's Trust Fund for Strategic Research (Grant No. SR/SCI/CHEM/21/01).

References

1 P. L. dos Santos, P. Stachelek, Y. Takeda and P. Pander, *Mater. Chem. Front.*, 2024, **8**, 1731–1766.
2 (*a*) A. Foucault-Collet, C. M. Shade, I. Nazarenko, S. Petoud and S. V. Eliseeva, *Angew. Chem., Int. Ed.*, 2014, **53**, 2927–2930; (*b*) M. Mei, B. Wu, S. Wang and F. Zhang, *Curr. Opin. Chem. Biol.*, 2024, **80**, 102469.
3 K. E. Borbas, in *Modern Applications of Lanthanide Luminescence*, ed. A. de Bettencourt-Dias, Springer International Publishing, Cham, 2023, pp. 35–65.
4 (*a*) H. Al-Sharji, R. Ilmi, W. F. Oliveira, B. S. Al-Saadi, J. D. L. Dutra, O. K. Abou-Zied, P. R. Raithby and M. S. Khan, *RSC Adv.*, 2024, **14**, 32573–32582; (*b*) S. I. Weissman, *J. Chem. Phys.*, 1942, **10**, 214–217.
5 (*a*) R. Ilmi, X. Xia, J. D. L. Dutra, G. S. Santos, L. Zhou, W. Y. Wong and M. S. Khan, *Eur. J. Inorg. Chem.*, 2025, e202400855; (*b*) L. Wang, Z. Zhao, C. Wei, H. Wei, Z. Liu, Z. Bian and C. Huang, *Adv. Opt. Mater.*, 2019, **7**, 1801256.
6 (*a*) R. Ilmi, X. Xia, J. D. L. Dutra, G. S. Santos, L. Zhou, W.-Y. Wong, P. R. Raithby and M. S. Khan, *ACS Appl. Electron. Mater.*, 2024, **6**, 2624–2638; (*b*) R. Ilmi, J. Wang, J. D. L. Dutra, L. Zhou, W.-Y. Wong, P. R. Raithby and M. S. Khan, *Chem. – Eur. J.*, 2023, e202300376; (*c*) R. Ilmi, X. Li, N. K. Al Rasbi, L. Zhou, W.-Y. Wong, P. R. Raithby and M. S. Khan, *Dalton Trans.*, 2023, **52**, 12885–12891.
7 A. Døssing, *Eur. J. Inorg. Chem.*, 2005, **2005**, 1425–1434.
8 D. Mara, F. Artizzu, P. F. Smet, A. M. Kaczmarek, K. Van Hecke and R. Van Deun, *Chem. – Eur. J.*, 2019, **25**, 15944–15956.
9 S. Susumu and W. Masanobu, *Bull. Chem. Soc. Jpn.*, 1970, **43**, 1955–1962.
10 Y.-F. Zhao, Y.-L. Zhao, F. Bai, X.-y. Wei, Y.-s. Zhou, M.-n. Shan, H.-h. Li, R.-j. Ma, X.-t. Fu and Y. Du, *J. Fluoresc.*, 2010, **20**, 763–770.
11 R. Ilmi, N. Hasan, J. Liu, D. Mara, R. Van Deun and K. Iftikhar, *J. Photochem. Photobiol., A*, 2017, **347**, 116–129.
12 H. Al-Sharji, R. Ilmi, N. K. Al Rasbi, A. Haque, P. R. Raithby and M. S. Khan, *J. Organomet. Chem.*, 2024, **1019**, 123309.
13 R. Ilmi and K. Iftikhar, *J. Coord. Chem.*, 2012, **65**, 403–419.
14 Stoe and Cie, *X-AREA and X-RED32*. Stoe & Cie GmbH, Darmstadt, Germany, 2002.
15 G. Sheldrick, *Acta Crystallogr., Sect. A: Found. Adv.*, 2015, **71**, 3–8.
16 G. Sheldrick, *Acta Crystallogr., Sect. C: Struct. Chem.*, 2015, **71**, 3–8.
17 C. F. Macrae, P. R. Edgington, P. McCabe, E. Pidcock, G. P. Shields, R. Taylor, M. Towler and J. van de Streek, *J. Appl. Crystallogr.*, 2006, **39**, 453–457.
18 A. Spek, *J. Appl. Crystallogr.*, 2003, **36**, 7–13.
19 L. Farrugia, *J. Appl. Crystallogr.*, 1999, **32**, 837–838.
20 (*a*) M. A. Spackman and D. Jayatilaka, *CrystEngComm*, 2009, **11**, 19–32; (*b*) D. Jayatilaka, S. K. Wolff, D. J. Grimwood, J. J. McKinnon and M. A. Spackman, *Acta Crystallogr., Sect. A: Found. Crystallogr.*, 2006, **62**, s90–s90.
21 P. R. Spackman, M. J. Turner, J. J. McKinnon, S. K. Wolff, D. J. Grimwood, D. Jayatilaka and M. A. Spackman, *J. Appl. Crystallogr.*, 2021, **54**, 1006–1011.
22 (*a*) M. Pinsky, C. Dryzun, D. Casanova, P. Alemany and D. Avnir, *J. Comput. Chem.*, 2008, **29**, 2712–2721; (*b*) D. Casanova, M. Llunell, P. Alemany and S. Alvarez, *Chem. – Eur. J.*, 2005, **11**, 1479–1494.
23 (*a*) A. J. M. Al-Karawi, A.-A. B. OmarAli, N. Dege and S. Kansız, *Chem. Pap.*, 2021, **75**, 3901–3914; (*b*) M. R. Albayati, S. Kansız, H. Lgaz, S. Kaya, N. Dege, I. H. Ali, R. Salghi and I.-M. Chung, *J. Mol. Struct.*, 2020, **1219**, 128518; (*c*) M. Morales-Toyo, S. Kansız, N. Dege, C. Glidewell, A. Fuenmayor-Zafra and N. Cubillán, *Chem. Phys.*, 2021, **544**, 111119.
24 W. T. Carnall, P. R. Fields and K. Rajnak, *J. Chem. Phys.*, 1968, **49**, 4424–4442.
25 R. Ilmi, A. B. Ganaie and K. Iftikhar, *J. Mol. Struct.*, 2018, **1173**, 990–999.
26 W. T. Carnall, P. R. Fields and B. G. Wybourne, *J. Chem. Phys.*, 1965, **42**, 3797–3806.
27 R. Ilmi and K. Iftikhar, *Inorg. Chem. Commun.*, 2010, **13**, 1552–1557.
28 (*a*) G. Stein and E. Würzberg, *J. Chem. Phys.*, 1975, **62**, 208–213; (*b*) M. Latva, H. Takalo, V. M. Mukkala, C. Matachescu, J. C. RodriguezUbis and J. Kankare, *J. Lumin.*, 1997, **75**, 149–169; (*c*) C.-L. Ho, H. Li and W.-Y. Wong, *J. Organomet. Chem.*, 2014, **751**, 261–285.

29 (*a*) Y. Zheng, L. Fu, Y. Zhou, J. Yu, Y. Yu, S. Wang and H. Zhang, *J. Mater. Chem.*, 2002, **12**, 919–923; (*b*) G. Sun, Y. Xie, Y. Wang, H. Zhang and L. Sun, *Angew. Chem., Int. Ed.*, 2023, **62**, e202312308; (*c*) Y. Xie, G. Sun, G. A. Mandl, S. L. Maurizio, J. Chen, J. A. Capobianco and L. Sun, *Angew. Chem., Int. Ed.*, 2023, **62**, e202301796.

30 M. D. Regulacio, M. H. Pablico, J. A. Vasquez, P. N. Myers, S. Gentry, M. Prushan, S.-W. Tam-Chang and S. L. Stoll, *Inorg. Chem.*, 2008, **47**, 1512–1523.

31 (*a*) S. Wang, J. Xu, J. Wang, K.-Y. Wang, S. Dang, S. Song, D. Liu and C. Wang, *J. Mater. Chem. C*, 2017, **5**, 6620–6628; (*b*) V. S. Sizov, D. A. Komissar, D. A. Metlina, D. F. Aminev, S. A. Ambrozevich, S. E. Nefedov, E. A. Varaksina, M. T. Metlin, V. V. Mislavskii and I. V. Taydakov, *Spectrochim. Acta, Part A*, 2020, **225**, 117503; (*c*) S. S. Mortensen, M. A. Marciniak Nielsen, P. Nawrocki and T. J. Sørensen, *J. Phys. Chem. A*, 2022, **126**, 8596–8605; (*d*) K. Lunstroot, P. Nockemann, K. Van Hecke, L. Van Meervelt, C. Görller-Walrand, K. Binnemans and K. Driesen, *Inorg. Chem.*, 2009, **48**, 3018–3026; (*e*) J. M. Stanley, C. K. Chan, X. Yang, R. A. Jones and B. J. Holliday, *Polyhedron*, 2010, **29**, 2511–2515.

32 H. F. Brito, O. L. Malta, M. C. F. C. Felinto, E. E. S. Teotonio, J. F. S. Menezes, C. F. B. Silva, C. S. Tomiyama and C. A. A. Carvalho, *J. Alloys Compd.*, 2002, **344**, 293–297.

33 Z. Li, J. Yu, L. Zhou, H. Zhang and R. Deng, *Inorg. Chem. Commun.*, 2008, **11**, 1284–1287.

34 R. Ilmi and K. Iftikhar, *Polyhedron*, 2017, **127**, 191–202.

35 (*a*) L. L. L. S. Melo, G. P. Castro and S. M. C. Gonçalves, *Inorg. Chem.*, 2019, **58**, 3265–3270; (*b*) K. Miyata, T. Nakagawa, R. Kawakami, Y. Kita, K. Sugimoto, T. Nakashima, T. Harada, T. Kawai and Y. Hasegawa, *Chem. – Eur. J.*, 2011, **17**, 521–528; (*c*) T. Ahmed, A. Chakraborty and S. Baitalik, *Inorg. Chem.*, 2024, **63**, 11279–11295; (*d*) R. Ilmi, D. Zhang, L. Tensi, H. Al-Sharji, N. K. Al Rasbi, A. Macchioni, L. Zhou, W.-Y. Wong, P. R. Raithby and M. S. Khan, *Dyes Pigm.*, 2022, **203**, 110300; (*e*) R. Ilmi, S. Kansız, N. K. Al-Rasbi, N. Dege, P. R. Raithby and M. S. Khan, *New J. Chem.*, 2020, **44**, 5673–5683; (*f*) R. Ilmi, S. Kansız, N. K. Al Rasbi, J. Husband, N. Dege and M. S. Khan, *Polyhedron*, 2023, **246**, 116673; (*g*) R. Ilmi, S. Kansız, N. Dege and M. S. Khan, *J. Photochem. Photobiol., A*, 2019, **377**, 268–281; (*h*) Y. Hasegawa, S.-i. Tsuruoka, T. Yoshida, H. Kawai and T. Kawai, *J. Phys. Chem. A*, 2008, **112**, 803–807; (*i*) A. B. Ganaie and K. Iftikhar, *J. Photochem. Photobiol., A*, 2022, **425**, 113715.

36 (*a*) Y. Gil, R. C. de Santana, A. S. S. de Camargo, L. G. Merízio, P. F. Carreño, P. Fuentealba, J. Manzur and E. Spodine, *Dalton Trans.*, 2023, **52**, 3158–3168; (*b*) P. Martín-Ramos, C. Coya, Á. L. Álvarez, M. Ramos Silva, C. Zaldo, J. A. Paixão, P. Chamorro-Posada and J. Martín-Gil, *J. Phys. Chem. C*, 2013, **117**, 10020–10030.

37 A. F. Rogozhin, L. I. Silantyeva, A. N. Yablonskiy, B. A. Andreev, I. D. Grishin and V. A. Ilichev, *Opt. Mater.*, 2021, **118**, 111241.

38 (*a*) Q. Sun, P. Yan, W. Niu, W. Chu, X. Yao, G. An and G. Li, *RSC Adv.*, 2015, **5**, 65856–65861; (*b*) P. Martín-Ramos, M. R. Silva, C. Coya, C. Zaldo, Á. L. Álvarez, S. Álvarez-García, A. M. Matos Beja and J. Martín-Gil, *J. Mater. Chem. C*, 2013, **1**, 2725–2734; (*c*) P. Martín-Ramos, C. Coya, V. Lavín, I. R. Martín, M. R. Silva, P. S. P. Silva, M. García-Vélez, A. L. Álvarez and J. Martín-Gil, *Dalton Trans.*, 2014, **43**, 18087–18096; (*d*) P. Martín-Ramos, V. Lavín, M. Ramos Silva, I. R. Martín, F. Lahoz, P. Chamorro-Posada, J. A. Paixão and J. Martín-Gil, *J. Mater. Chem. C*, 2013, **1**, 5701–5710; (*e*) P. Martín-Ramos, I. R. Martín, F. Lahoz, S. Hernández-Navarro, P. S. Pereira da Silva, I. Hernández, V. Lavín and M. Ramos Silva, *J. Alloys Compd.*, 2015, **619**, 553–559; (*f*) P. Martín-Ramos, P. S. P. Silva, P. Chamorro-Posada, M. Ramos Silva, B. F. Milne, F. Nogueira and J. Martín-Gil, *J. Lumin.*, 2015, **162**, 41–49; (*g*) G. Brito-Santos, B. Gil-Hernández, I. R. Martín, R. Guerrero-Lemus and J. Sanchiz, *RSC Adv.*, 2020, **10**, 27815–27823; (*h*) P. Martín-Ramos, M. Ramos Silva, F. Lahoz, I. R. Martín, P. Chamorro-Posada, M. E. S. Eusebio, V. Lavín and J. Martín-Gil, *J. Photochem. Photobiol., A*, 2014, **292**, 16–25.